MTLA 30 (2023) 101813

Contents lists available at ScienceDirect

Materialia

journal homepage: www.elsevier.com/locate/mtla

Full length article

On the formation of pileups during nano-scratching of Inconel 718 produced using additive manufacturing

Mustafa Rifat [a], Darren C. Pagan [b], Edward C. DeMeter [a], Saurabh Basu [a,*]

[a] *Harold and Inge Marcus Department of Industrial and Manufacturing Engineering, Penn State University, University Park, PA, USA*
[b] *Department of Materials Science and Engineering, College of Earth and Mineral Sciences, Penn State University, University Park, PA, USA*

ARTICLE INFO

Keywords:
Inconel 718
Nano-scratch test
Pile-up behavior
Hardening

ABSTRACT

The objective of this work is to understand the role of microstructure on pileup formation during nano-scratching of additively manufactured nickel superalloy, Inconel 718 (IN718). Scratches with median depths of ~50 nm were made on as-received and solution annealed IN718 under the action of small normal forces using a spheroconical diamond indenter. The surface profiles of these scratches were then quantified using atomic force microscopy. The as-received IN718 showed a positive correlation between pileup height, and scratch depth. In contrast, the solution annealed IN718 specimen exhibited a negative correlation between pileup height, and scratch depth. Analysis of this observation involved experimental quantification of microstructure using electron back scatter diffraction, quantitative atomic force microscopy, in addition to complementary finite element simulations. Following analysis, we propose that this switchover originates due to differences in strength, hardening, and deformation localization characteristics of as-received and solution annealed IN718.

1. Introduction

Laser powder bed fusion (LPBF) is a popular alloy additive manufacturing (AM) method to create near-net shape parts. Prior to end use, these parts typically must undergo significant post-processing. Heat treatment(s) are performed for purposes of stress relieving, solution annealing, and/or precipitation hardening to achieve strength and ductility requirements. Parts must also often undergo primary machining to realize functional surfaces that meet geometric and roughness texture requirements and often secondary, abrasive machining processes to realize non-functional surfaces that also meet roughness texture requirements. Secondary machining is necessitated by originated surfaces that are often as rough as $R_a = 25$ μm and with finish requirements of $R_a = 1.5$ μm or less. As primary and secondary machining processes can be interjected anywhere in the manufacturing sequence, determining ideal placement (i.e., before or after heat treatment) to produce optimized surfaces can greatly enhance final components. One way to explore this is the nano-scratch test, which in many ways mimics the mechanics of a single grit interacting with the metal. In this work, we present nano-scratch results for AM Inconel 718 nickel superalloy (IN718) to aid the optimization of full LPBF component production.

In the nano-scratch process, a nano-indenter is advanced along a surface while under a normal force [1–3]. Two raised pile-ups are formed on either side during this process as the material plastically deforms and is pushed out of the path of the indenter. This plasticity is mediated by dislocation motion, twinning, or both depending on the material, loading rate, and temperature [1,4]. At larger scratch depths, the local fracture toughness of the material can be exceeded, leading to intermittent fracture [4,5]. The propagation of dislocations to the surface has been identified as an important mechanism of formation of pileup during nano-indentation [6–8], and nano-scratching [9]. To this end, a defect-free surface in the vicinity of the scratch provides an energetically convenient sink for dislocations [10–12]. However, the presence of forest dislocations, solute atoms, and precipitates in advanced metallic systems that often feature engineered combinations of these microstructural variables undergoing scratching can alter the hardening and subsequent flow behavior, and thereby influence the characteristics of the resulting pileup. In addition, the fact that scratch behavior is near the free surfaces can also significantly alter plastic deformation behavior in comparison to bulk deformation processes [1,13]. Dislocations that escape from the surface to create pileups naturally do not increase the hardening rate by becoming pinned or becoming part of larger dislocation structures. This effect is presumably amplified in shallow scratch depths where a larger proportion of dislocations generated escape to the surface.

During LPBF of IN718, significantly different microstructures are generated in comparison to wrought counterparts. Rapid solidification causes segregation of larger atoms such as Nb, and Mo. Prior studies

---

* Corresponding author.
E-mail address: sxb514@psu.edu (S. Basu).

https://doi.org/10.1016/j.mtla.2023.101813
Received 4 January 2023; Accepted 28 May 2023

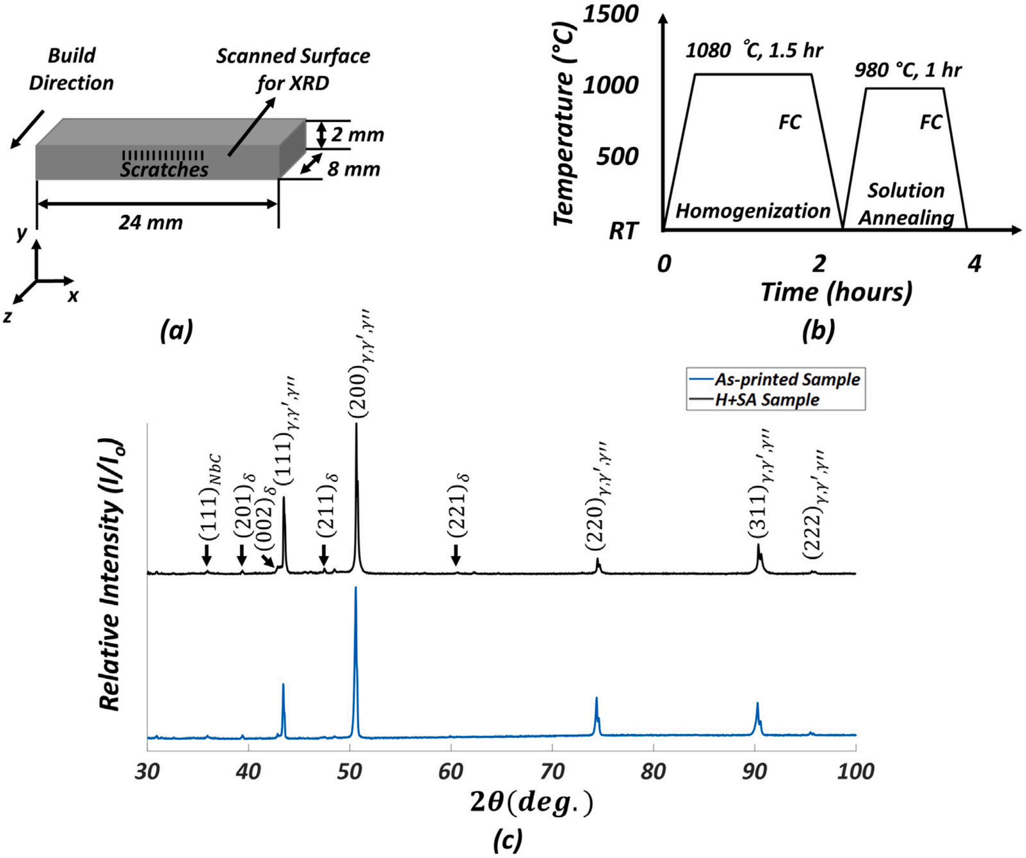

Fig. 1. (a) Schematic of the specimen and the location of scratches; (b) Temperature profile of heat-treatment procedure (RT= Room Temperature, FC= Furnace Cooling); (c) X-ray Diffraction pattern of as-received and heat-treated (H+SA) specimens.

have shown that this results in the presence of a brittle Laves phase [14] which is generally detrimental to mechanical behavior. Nonetheless, the stress relief step has an effect similar to homogenization [15,16], wherein the Laves phases are partially dissolved from long/slender and brittle morphology to the more fracture resilient [14] spherical morphology. Subsequent solution annealing results in formation of the δ phase (Ni_3Nb) precipitates close to grain boundaries, and eventually within the matrix itself. The preferential dissolution of the δ phase near the grain boundary occurs due to easier diffusion of Nb atoms there [17]. Herein, the homogenization step acts an important precursor; it redistributes the Nb atoms from the Laves phase particles to the γ Ni matrix grain interiors. These various phases and changes to local composition that are produced during LPBF and subsequent heat treatment of IN718 alloy microstructure all can effect hardening characteristics and pileup behavior.

Here, we present analyses of pileup behavior during nano-scratching in IN718 nickel superalloy with varied microstructure composition. Specifically, we look at an IN718 alloy that was produced using LPBF. The behavior of specimens was studied in their: (1) as-received state which comprised a manufacturer recommended stress relief step after extraction from the additive manufacturing platform, and, (2) subsequent homogenization + solution annealed state.

2. Materials and methods

Nano-scratch tests were performed on two IN718 substrates. (see Fig. 1a) The first substrate was produced by LPBF and subsequently stress relieved at a temperature of 1065° ± 12° C for 90 min [18]. The second was also homogenized and solution annealed (H+SA) prior to scratching. The H+SA heat treatment used was adapted from Ref. [19,20] and comprised two steps: (i) homogenization at $1080°C$ for 1.5 h. followed by furnace cooling to room temperature, and (ii) solution annealing at $980°C$ for 1 hr. followed by furnace cooling to room temperature (see Fig. 1b). This heat-treatment was carried out in Argon environment and resulted in precipitation of the δ phase, which was deduced by X-ray Diffraction (XRD) with a copper source over a Bragg angle range $2\theta = 30 - 100°$ and a step size of 0.026°. Fig. 1c shows the $(002), (211), (221)$ δ-phase peaks at $2\theta = 43.1°, 47.5°, 60.7°$ in the H+SA specimen respectively [21,22], which were not prominent in the as-received specimen. Energy Dispersive X-ray Spectroscopy (EDS) was performed on the specimens to identify precipitates in the matrix in as-received and H+SA specimens. For this, the surfaces of the substrates perpendicular to the build direction were mechanically polished to a 0.04 μm colloidal silica step prior to scratching. Some polished specimens were etched with Kalling's 2 reagent. Fig. 2a show the EDS mapping of as-received sample. AM IN718 samples in their as-received state exhibited Nb segregation in the matrix, characterized by the presence of Nb rich zones. The homogenization + solution annealing heat treatment [16] resulted in precipitation of needle shapes δ Ni_3Nb close to grain boundaries (Fig. 2b). Some metal carbides (MCs) were also inferred in the microstructure, both before and after H+SA treatment. The MCs can withstand higher temperature range with a solvus of 1040 °C–1200 °C [23], wherein their presence before, as well as after heat treatment is not surprising.

For scratching the as-received specimen, a force of 1 mN was imposed on a sphero-conical tip with tip radius $r = 0.5$ μm and included cone angle 90° to produce an indent on this polished substrate. This was done in Hysitron Triboindenter TI900 equipment. The indenter was then advanced under the influence of the aforementioned 1 mN force across a distance of 10 μm over a duration of 15 s. A total of 14 such scratches were made each spanning 1–3 grains. The locations of these scratches with respect to the vertical free surface that resulted from AM

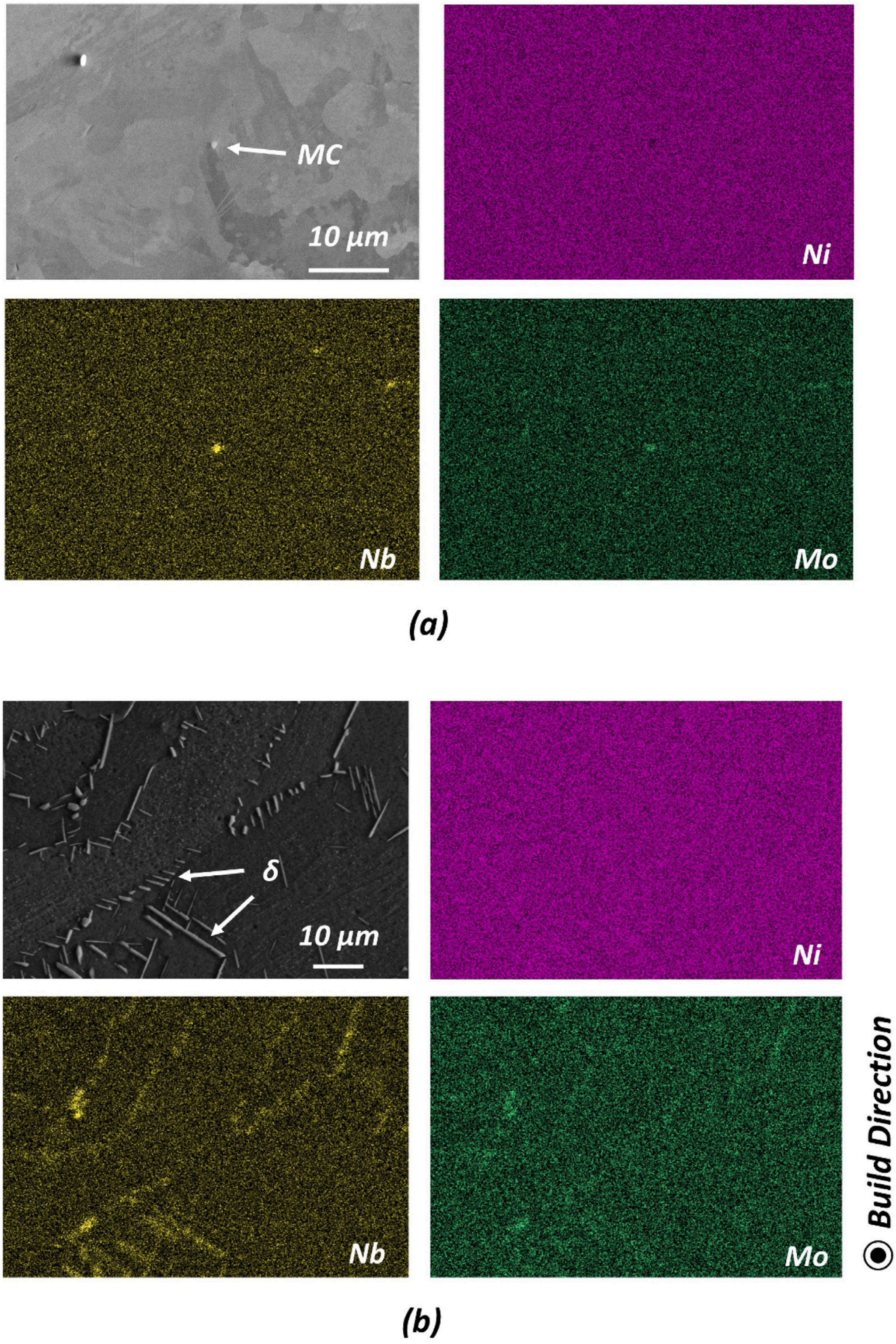

Fig. 2. Energy Dispersive X-ray Spectroscopy.

is schematically illustrated in Fig. 1a. To identify the crystallographic orientations of these grains, Electron Back Scattered Diffraction (EBSD) was performed. A coarse resolution (0.55 μm) was used prior to the scratch and a fine resolution (80 nm) was used after the scratch. Following the scratch process, their topographies were characterized using Atomic Force Microscopy (AFM). From these AFM scans, line profiles with inter-spacing of 24 nm (~400 lines per scan) were extracted in a direction perpendicular to the scratch. From each profile, maximum scratch depth, and maximum adjacent pile-up height were extracted. Nano-scratch tests were performed on the H+SA specimen. Eleven

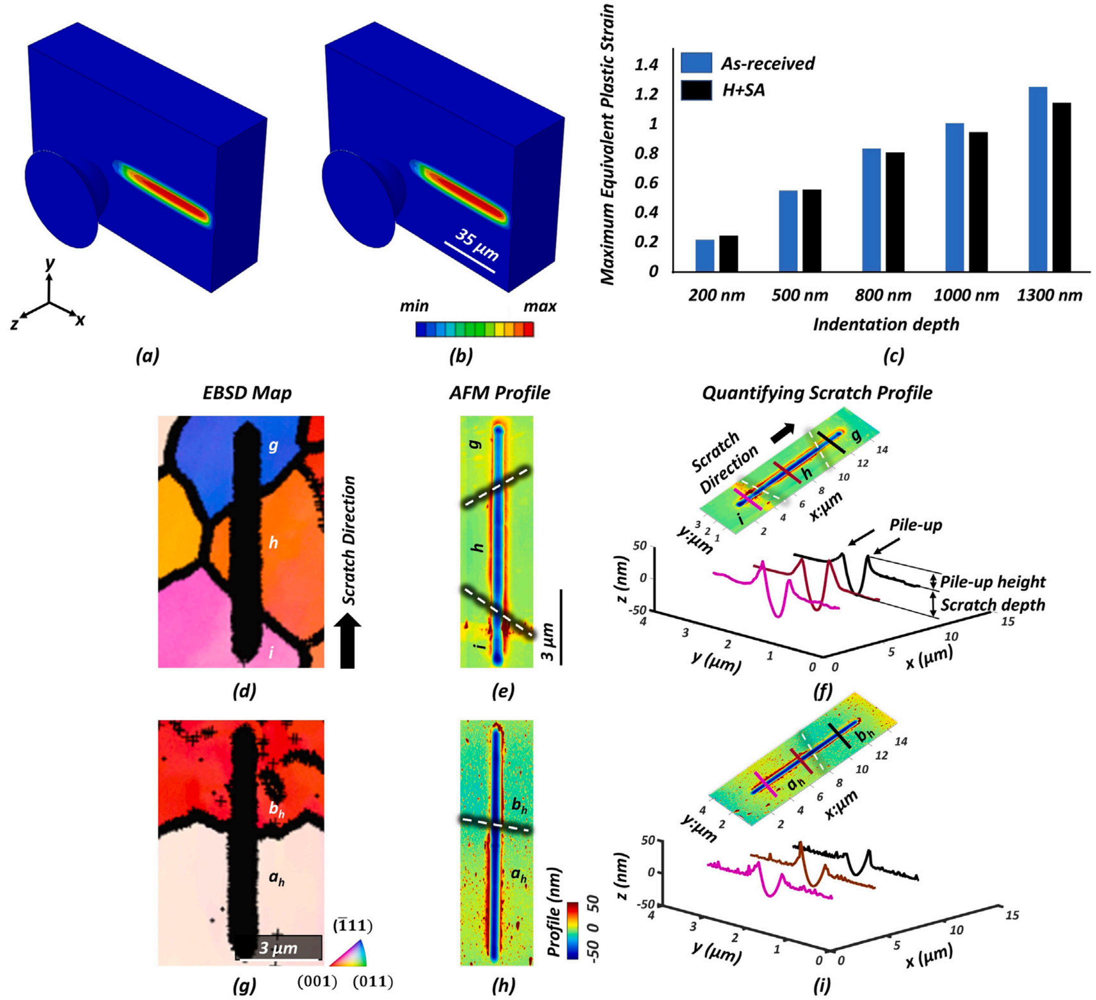

Fig. 3. Effective plastic strain field (a), (b) are shown from the FEA model for 500 nm indentation depth for the as-received and heat-treated specimens, respectively. The maxima of equivalent plastic strain field for different indentation depths are shown in (c). Orientation Imaging microscopy (d), (g), Atomic Force Microscopy (e), (h), and schematic of scratch characterization procedure (f), (i), from AFM micrograph are shown in as-received (middle row), and heat treated (bottom row) specimens. The dark black lines in (d), and (g) are grain boundaries featuring misorientation > 15° across neighboring zones. These boundaries are shown using white dashed lines in the atomic force microscopy maps (e), (h). The pink, brown and black lines in the AFM image of (f), (i) show example of three instances that were extracted from the scratch profiles to quantify pile-up height and scratch depth.

scratches were made in this specimen with a 2 mN normal force and the remaining nano-scratch parameters matched those used for the as-received IN718 specimen.

3. Numerical modeling

An isotropic plasticity finite element model was utilized to estimate the deformation conditions, particularly the local stress and final strain conditions, in the as-received and H+SA condition. These estimates were used to help contextualize the observed pileup behavior in the two specimen conditions. A spherical diamond tip with 20 μm radius and a workpiece of $150\ \mu\text{m} \times 40\ \mu\text{m} \times 100\ \mu\text{m}$ were used in the model. Several scratch depths, e.g., 200 nm, 500 nm, 800 nm, 1000 nm and 1300 nm were simulated. A speed of $0.67\ \mu\text{m/s}$ was used that matched the scratch speed of our experiments. The IN718 sample was modeled with density, $\rho = 9000\ \text{kg/m}^3$, a nominal elastic modulus, $E = 200$ GPa and Poisson's ratio, $\nu = 0.29$. The indenter was modeled with density, $\rho = 3530\ \text{kg/m}^3$; elastic modulus, $E = 1210$ GPa and Poisson's ratio, $\nu = 0.22$. Linear hexahedral (C3D8R) and quadratic tetrahedral (C3D10) elements were used in modeling the workpiece and indenter, respectively. The coefficient of friction between the indenter and the substrate was set to $\mu = 0.15$ to reflect interaction between diamond tip and nickel. Johnson Cook hardening law was implemented to model the deformation behavior. The parameters of the hardening law for the as-received condition was $[A, B, C, n, m] = [450\ \text{MPa}, 1700\ \text{MPa}, 0.017, 0.65, 1.3]$ same as that used previously for the as-received material by the authors [18]. The parameters of the hardening law for the H+SA condition were $[A, B, C, n, m] = [450\ \text{MPa}, 1798\ \text{MPa}, 0.0312, 0.91, 0]$ as per Ref. [24].

Figs. 3a and 3b show the final estimated strain field for 500 nm indentation depth simulation for as-received and H+SA specimen, respectively. Maxima for the equivalent plastic strain field for indentation depths= 200 nm, 500 nm, 800 nm, 1000 nm and 1300 nm were 0.2165, 0.5497, 0.834, 1.007, 1.254 for the as-received specimen, respectively. For the H+SA specimen these maxima values were 0.2439, 0.5569, 0.8082, 0.9458, 1.144, respectively. The maximum values of equivalent plastic strain are smaller in H+SA specimens compared to the as-received state for the larger scratch depths as observed in Fig. 3c. Nonetheless, both sets of simulations produced a positive correlation between maximum strain and scratch depths, which is in line with observations of fracture at larger depth values [4,5].

4. Results

Figs. 3d–3f summarize an instance of the nano-scratches produced on as-received IN718. These sub-figures comprise orientation field

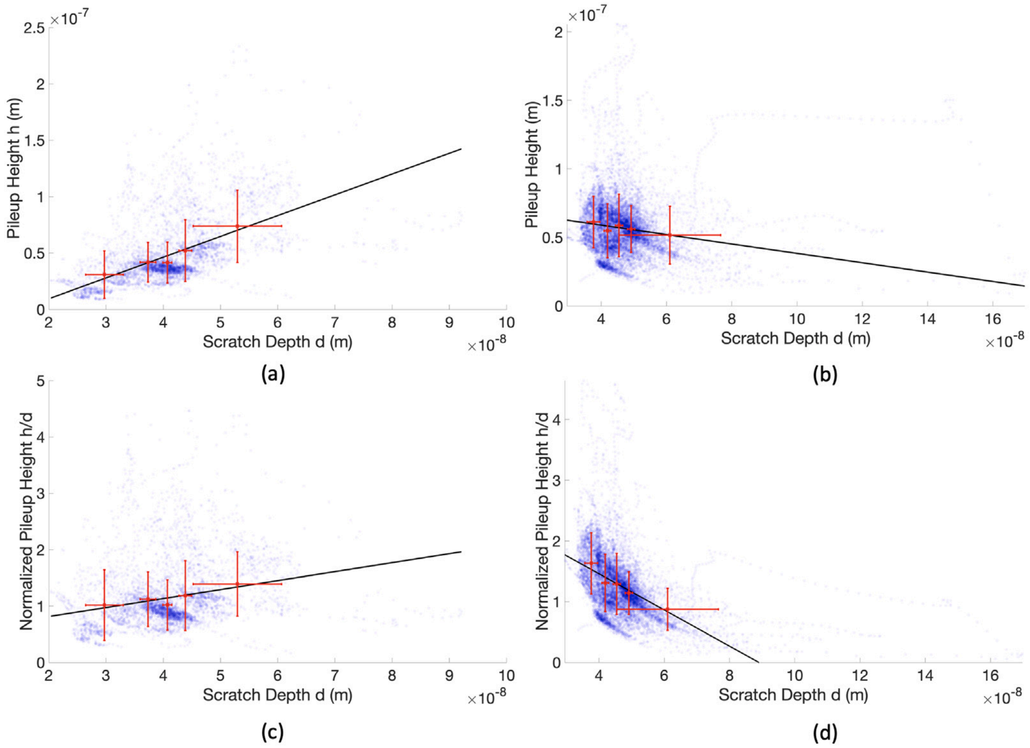

(a) (b)

(c) (d)

Fig. 4. Pile-up height h as a function of scratch depth d for the: (a) as-received specimen, (b) H+SA specimens. Normalized pileup height as a function of scratch depth for: (c) as-received specimen, (d) H+SA specimens. No down-sampling was performed to produce these figures.

characterized with EBSD, AFM, and procedure of quantification of scratches, respectively. The dashed lines in Fig. 3e label the intersecting grain boundaries. The scratch profiles exhibited considerable variations in depth under constant perpendicular load with respect to the local grain orientation. An instance of this phenomenon is obvious during transition from grain $i \rightarrow h \rightarrow g$ (see Fig. 3e) wherein the scratch depth increased from ∼36.43 nm to ∼40.89 nm, and then decreased to ∼30.81 nm, respectively. Note, this variation occurred under the action of the consistent normal force of 1 mN. Figs. 3g–3i show the corresponding images for an instance of the scratches produced on the thermally treated IN718. Here, the scratch crosses a grain boundary separating grains a_h and b_h. The corresponding scratch depths were 44.56 nm and 46.79 nm, respectively.

Maxima of pileup heights h were extracted from the individual scratch profiles, and their correlations were characterized with respect to corresponding scratch depths d in the same profile. This is shown in Fig. 4a for the as-received specimen, and Fig. 4b for the H+SA counterpart. In both cases, scratch depths d within similar ranges, viz., $d \in (25\ \text{nm},\ 80\ \text{nm})$, and $d \in (33\ \text{nm},\ 80\ \text{nm})$, respectively, were seen. Further, both specimens exhibited median pileup heights of $\tilde{h} \sim 50$ nm. A small number of instances featuring higher scratch depths $d \in (80\ \text{nm},\ 160\ \text{nm})$ were also observed, but these were not representative of the general behavior of scratching that dominated the two substrates.

The coefficient of determination of the pileup height was quantified by modeling it as a linear function of the scratch depth. To isolate biases that may arise from noise, the data was distributed into $n = 3 - 10$ quintiles with respect to the scratch depth, wherein each bin comprised fractions $1/3 - 1/10$, respectively, of the data population. Subsequently, linear fits were found for the corresponding quintile means of pileup height, and scratch depth, wherein these lines comprised between 3-10 data points which emulated the real physical behavior. The corresponding coefficients of determination are summarized in Table 1 for the as-received, and H+SA specimens. Figs. 4a, 4b show the fitted lines for the case with $n = 5$ quintiles.

In general, the as-received specimen exhibited a positive correlation between pile-up height h, and scratch depth d. Each of the $n = 3 - 10$ quintiles consistently exhibited a coefficient of determination $R^2 \geq 0.92$. On the contrary, the H+SA specimen consistently exhibited a negative correlation between the maximum pileup height, and scratch depth. Further, this specimen exhibited a decline in coefficient of determination to smaller values, e.g., $min\{R^2\} = 0.64$ for $n = 9$, suggesting that a simple model that correlates pileup heights with corresponding scratch depths is not sufficient to capture the relevant physical behavior. These differences suggest a transition in the mechanism underlying pileup generation across our as-received, and H+SA heat treated IN718, which originated from AM. A positive correlation across pile-up heights, and scratch depths implies that a deeper scratch produced a taller pileup, wherein the extra material displaced during the scratch reappeared at the free surface. However, a negative correlation implies that a deeper scratch produced a shorter pileup, wherein the extra material engaged by the deeper scratch was displaced with a mechanism that was different than the as-received counterpart.

To probe this further, the evolution of the normalized pileup depth h/d was quantified with respect to local scratch depth d. This quantification was also done by segregating the data points into quintiles $n = 3 - 10$, and fitting a line between quintile means of normalized pileup height h/d, and scratch depth d. The as-received specimen exhibited a considerable positive correlation between the normalized pileup height, $\frac{h}{d}$, and scratch depth d. The coefficient of determinations R^2 of the linear fits were always found to be larger than 0.64 for quintiles $n = 3 - 10$. In comparison, the H+SA specimen exhibited a dominantly negative correlation between parameters $\frac{h}{d}$, and d. The R^2 values for quinitiles $n = 3 - 10$ consistently exhibited $R^2 \geq 0.93$. Figs. 4c and 4d show this relationship for $n = 5$ quintiles for as-received and H+SA specimens, respectively. The coefficients of determination for various quintiles are shown in Table 1.

Table 1
Coefficients of determination obtained for linear fits between pileup heights, and independent variables for quintile levels $n = 3 - 10$.

Material state	Independent variable	Dependent variable	Quintile, n							
			3	4	5	6	7	8	9	10
As-received	Depth, d	Pile-up height h	0.93	0.93	0.94	0.93	0.93	0.92	0.92	0.92
H+SA	Depth, d	Pile-up height h	0.95	0.85	0.69	0.76	0.72	0.74	0.64	0.68
As-received	Depth, d	Normalized Pile-up height $\frac{h}{d}$	0.70	0.74	0.77	0.71	0.69	0.65	0.64	0.65
H+SA	Depth, d	Normalized Pile-up height $\frac{h}{d}$	0.99	0.96	0.94	0.95	0.94	0.94	0.93	0.93

5. Discussion

5.1. Effect of pre-existing dislocation density

The reported variations in the correlation between scratch depth and the pileup height are rationalized through analysis of the features of the gamma (γ) matrix of IN718 including its dislocation density field, precipitates, and interstitials. In our as-received state, the grains in the γ matrix featured an average Geometrically Necessary Dislocation (GND) density of $2.16{\times}10^{14}/\mathrm{m}^2$. In comparison, the material in the heat-treated state featured a marginally lower average GND density of $2.11{\times}10^{14}/\mathrm{m}^2$. These values refer to the magnitude of the Nye tensor that were quantified using EBSD and the routine 'ebsd.curvature' available in the open source MTEX toolbox [25]. The routine is based on the formulation in Ref. [26]. This formulation quantifies the curvature of the planar orientation field, and thereby, only provides an estimate of the true GND density. Further, it assumes the contribution to curvature due to elastic strains [27] are negligible. Assuming proportionality between GND and total dislocation densities, this small difference in dislocation density across the two states rules out dislocation-forest hardening mechanisms as the originator of the change in pileup characteristics across our specimens. The relatively high values of GND density also rule out any role of Discontinuous Dynamic Recrystallization (DDRX) on pileup formation as the occurrence of DDRX would generally lower measured GND density as recrystallization proceeds [28].

5.2. Effect of scratch tip radius

Wear of the scratch tip can produce changes in the mechanics of scratching, that can manifest altered pileup formation. To investigate this possibility, the indenter tip radii were estimated from the valleys of the scratch cross-sections that were characterized using AFM. This radii quantification was performed by fitting semicircles to the AFM cross-section profiles that were obtained from the vicinity of the deepest points in the scratch. Ten equally spaced readings were characterized along the length of ten scratches from both specimen types and are listed in Table 2.

The values in Table 2 list the mean and standard deviation of the radii for the ten readings of every scratch. We note that these radii are only remnants of the plastic deformation phenomena that took place during the scratch and that there will be some deviation between the measured radii and true indenter radius due to recovered elastic deformation. Nonetheless, the measurements generally indicate that the indenter tip did not lose its sharpness during the course of our nano-scratch experiments. While changes caused by evolution of the indenter tip during scratching are expected, we believe these changes to be relatively minor and do not affect the general results presented.

Table 2
Valley radii at the vicinity of the deepest points of scratches in the as-received and H+SA specimen.

Scratch	As-received Specimen Valley Radii (nm)	H+SA Specimen Valley Radii (nm)
1	679 ± 102	556 ± 47
2	554 ± 44	527 ± 12
3	611 ± 48	505 ± 36
4	510 ± 36	526 ± 23
5	621 ± 45	518 ± 26
6	621 ± 44	538 ± 13
7	539 ± 66	510 ± 32
8	558 ± 25	553 ± 25
9	520 ± 31	518 ± 23
10	524 ± 17	552 ± 19

5.2.1. Effect of precipitates

Additive manufacturing of IN718 produces segregation of Nb, and Mo during solidification [14]. This results in brittle Laves phase that assume a fracture resistant spherical morphology after the stress relief step used in this work. These precipitates can cause gradients in plastic deformation fields in the vicinity of the tip during nano-scratching. In the same vein, the δ phase precipitates in our H+SA specimen can also produce gradients in deformation fields. To quantify these effects, the coefficient of variation of scratch depth was characterized from their AFM profiles. This involved quantifying the sample standard deviation of scratch depth $\hat{\sigma}_d$, and dividing that with the corresponding mean of the scratch depth profile $\langle d \rangle$. Compilation of all scratch depths individually from the line profiles extracted from AFM scans (see Fig. 3) was performed prior to this characterization. The as-received specimens exhibited a coefficient of variation $COV_{as-received} = \hat{\sigma}_d / \langle d \rangle = 0.2091$. In comparison, the H+SA specimen exhibits a marginally larger coefficient of variation $COV_{H+SA} = 0.2263$. Further, the H+SA specimen required double the normal force 2 mN despite exhibiting similar scratch depths as the as-received specimen that required a force 1 mN. The H+SA specimen also exhibited a larger lateral force of $1.62 \times 10^{-4} \pm 1.67 \times 10^{-5} N$, which was about 4× compared with the as-received specimen that exhibited $4.33{\times}10^{-5} \pm 1.22{\times}10^{-5} N$. These results generally indicate δ particles act as obstacles to scratching.

The enhanced resistance that the H+SA specimen offers to scratching can be due to microplastic phenomena spurred by δ precipitates. These can produce sharper deformation gradients under the action of the approaching scratch tip which then lifts up under the action of the consistent normal force. Repeated occurrence of this phenomenon during several encounters of the scratch tip with δ precipitates can produce larger coefficients of variation of scratch depth in the H+SA condition.

Evidence of this behavior was probed in the microstructural characteristics left in the wake of the scratch. For this, instances that involved direct engagement of the scratch tip with δ precipitates were

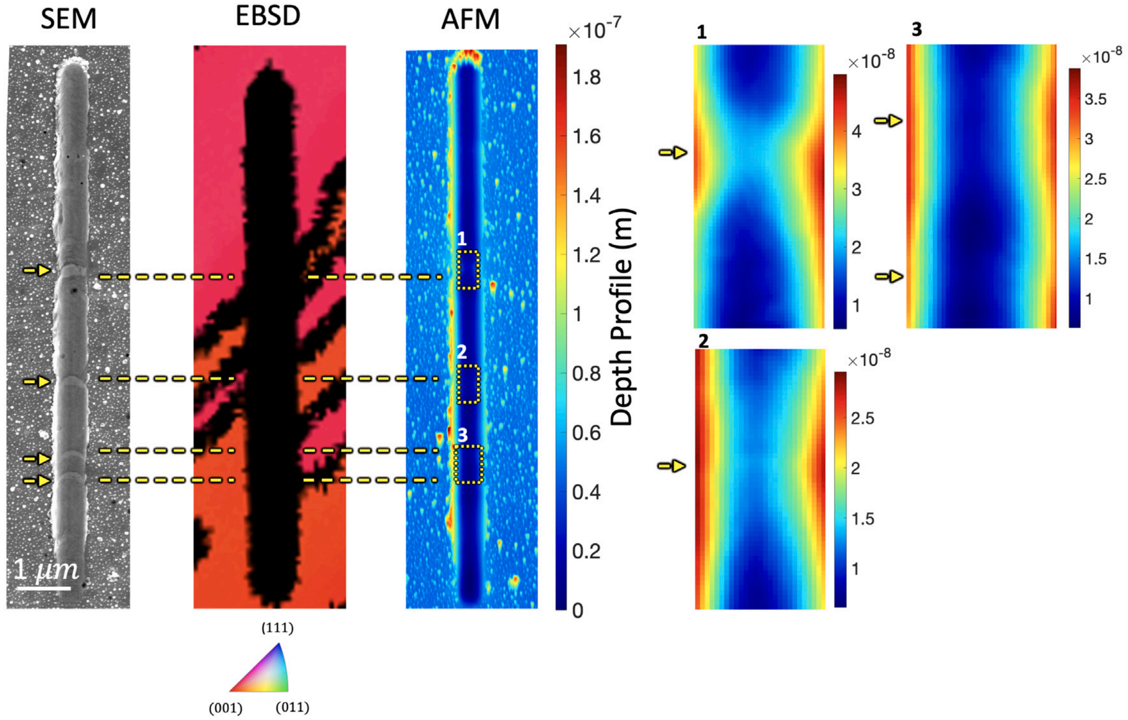

Fig. 5. Evidence of δ phase and its influence of mechanics of scratching. Insets 1, 2, and 3, on the right show magnified views of the AFM scans of the zones shown in dashed yellow boxes. The exact locations of the delta phases are highlighted using yellow arrows in these insets.

investigated. Note, δ precipitates were not indexed directly via Kikuchi diffraction during orientation imaging microscopy. However, evidence of their presence was found in SEM characterization, in OIM characterization (as corresponding zones that feature poor confidence index), and as corresponding undulations in the AFM scans. Fig. 5 shows instances of these effects in the H+SA specimen. The evidence of the δ phase particles is highlighted using yellow dashed lines. These δ phase particles act as obstacles to the scratch tip. Consequently, the tip lifted up while traversing over them under the action of the constant normal force (2 mN). This is evidenced four times during the same scratch that is shown in Fig. 5. Similar evidence of δ phase particles was found in every instance of scratches in our heat treated specimens that happened to traverse through a grain boundary. The presence of δ phase particles also results in the absence (or recession) of a pileup in neighboring zones. It was also seen that such features were consistently absent in all scratches performed in this work that were far away from grain boundaries.

In total, the observed differences in pileup behavior between the two substrates suggest that changes to the microstructure which result from heat treatment fundamentally alters the plastic deformation behavior of IN718 with respect to its as-received state. The δ precipitates in the H+SA specimen can pin dislocations and reduce their mean free paths wherein the odds that a dislocation is able to reach the surface during scratching are reduced. This phenomenon effectively prevents/subdues localization of slip in bands that produce slip traces, which were more frequently observed in our as-received IN718 specimen that lacked δ precipitates, and a homogenized solute atmosphere. A similar effect was observed recently in homogenized IN718, compared with its aged counterpart [29]. In this work, it was observed that the dislocation pinning effect in homogenized IN718 reduced the intensity of slip bands that resulted in the first cycle of fatigue loading, thereby increasing its fatigue efficiency (ratio of fatigue strength to the yield strength), compared with the aged counterpart [29].

We envision that the dislocations trapped by obstacles, e.g., δ precipitates in our homogenized IN718 specimens result in residual elastic deformation to ensure compatibility, which then produces the negative correlation between pileup height, and scratch depth. Similar phenomena has been observed during nano-indentation at smaller E/Y regimes, where E is the Young's modulus, and Y is the yield strength [30,31]. Nanoindentation was used to characterize a similar metric, viz., $\frac{E}{H}$ in the specimens used in this work. Here, E is the Young's modulus, and H is the hardness of the specimen. Ten nanoindents were performed using a Berkovich indenter at ten different load levels ranging between 1 mN – 10 mN. For each load level, nanohardness and reduced Elastic Modulus (E_r) were calculated. E_r is the elastic modulus of the specimen-indenter system which is related to the Elastic Modulus and Poisson ratio of the specimen (E_s and v_s, respectively) and indenter (E_i and v_i, respectively). From the reduced Elastic Modulus the specimen Elastic modulus was calculated using the following relation [32]:

$$E_s = \frac{1 - v_s^2}{\frac{1}{E_r} - \frac{1 - v_i^2}{E_i}} \tag{1}$$

According to Hertzian theory of contact mechanics, reduced Elastic Modulus is derived from the nanoindentation tests using the relation [32,33]:

$$E_r = \frac{1}{2}\sqrt{\frac{\pi}{A_p}}\frac{dP}{dh} \tag{2}$$

Here, $\frac{dP}{dh}$ is the slope of the unloading part of the indentation load–displacement curve at the maximum displacement point ($h = h_{max}$) and A_p the projected area of contact. Projected area was calculated using the tip area function of the nanoindenter ($A_p = C_o h_c^2 + C_1 h_c + C_2 h_c^{0.5} + C_3 h_c^{0.25} + C_4 h_c^{0.125} + C_5 h_c^{0.0625}$) where $C_o - C_5$ are constants and h_c is the contact depth during indentation full load. This tip area function was separately characterized prior to measurement of elastic moduli of the as-received, as well as the heat treated specimens. Once the value of E_r was derived from the test, Eq. (1) was used to quantify the E_s value for the different load levels considering $v_s = 0.29, v_i = 0.07$ and $E_i = 1140$ GPa. Lastly, nanohardness (H) was calculated using $H = \frac{P}{A_p}$. Fig. 6 shows the hardness determined from the ten

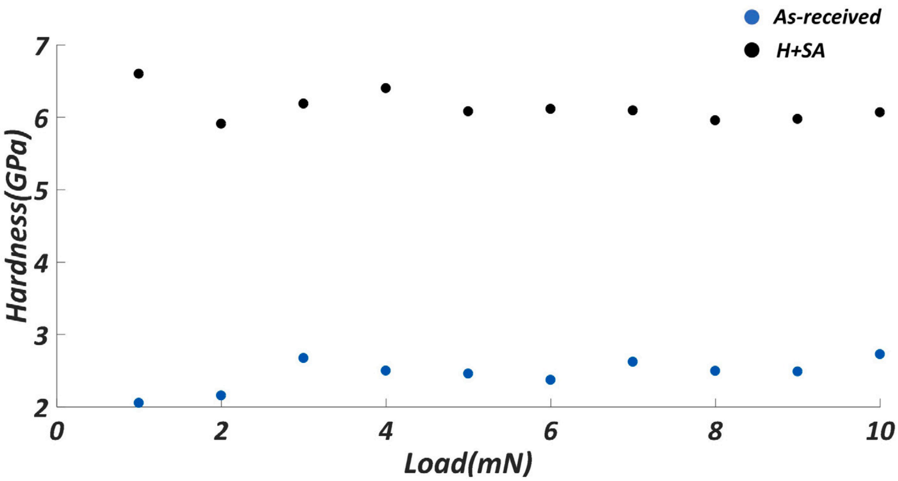

Fig. 6. Nano-indentation hardness as a function of load.

indentations in the as-received and H+SA specimens. The as-received specimen exhibited a Young's modulus of $E = 172 \pm 17$ GPa, and a hardness of $H = 2.45 \pm 0.21$ GPa. It exhibited $\frac{E}{H} = 71.2 \pm 12.5$. The heat treated (H+SA) specimen exhibited Young's modulus of $E = 219 \pm 12$ GPa, and a hardness of $H = 6.14 \pm 0.21$ GPa. It exhibited $\frac{E}{H} = 35.7 \pm 2.6$. This suggests that the H+SA conditions studied in this work is likely to form larger residual stresses which can contribute to the switchover in correlation between pileup heights and scratch depths, e.g., from positive to negative, across as-received and H+SA conditions respectively. Note, indentation size effects were not seen in this load range (see Fig. 6). This suggests that the characteristic length of these specimens was very small. This can happen due to pre-existing dislocation densities [34]. In addition, the precipitates in the matrix can produce local strain gradients. This can cause a rapid increase in dislocation densities during plastic straining [35], thereby effectively decreasing the characteristic length further.

The formation of pileup and sink-in during indentation of a material is mechanistically governed by the ratio between its hardness H and elastic modulus E, i.e., H/E [36,37]. This parameter is often utilized to rationalize the transition from pileup to sink-in behavior and thresholds that govern this transition have been found to depend on the hardening exponent N of the material. This exponent refers to that in the Hollomon equation that relates yield strength Y to true strains ϵ as $Y = K\epsilon^N$. For instance, for a material featuring hardening exponent $N = 0.1$, a threshold $Y/E \sim 0.01$ has been proposed to govern this transition [37]. The IN718 model parameters used in this work correspond to $N = 0.19$, and $N = 0.14$, for the as-receieved and H+SA specimens, and feature thresholds of $Y/E \sim 0.009$, $Y/E \sim 0.006$, repsectively, that would govern the transition between pileup and sink-in behavior. To convert this to the ratio $\frac{H}{E}$, Lockett's result can be used which relates the yield strength of the material to its hardness as $H = \frac{Y}{\sqrt{3}}(1.41 + 2.72\theta)$ [38,39], where $\theta(= 65.72°)$ is the half angle of the Berkovich indenter. This results in the threshold ratio $\frac{H}{E} \sim 2.6\frac{Y}{E} = 0.017$, and, 0.022, for our as-received, and H+SA specimens. This is similar to numerical results obtained by Marx and Balke [40] and empirical results obtained by Burik et al. in steel [41], and by Hassaan et al. in Ti alloy Ti–5Al–2.5Sn [42]. These trends are in line with observations made in this work. Our as-received specimens exhibit $H/E \sim 0.014 < 0.017$ and form pileups featuring a positive correlations between pileup height and scratch depth. On the other hand, our H+SA specimens exhibit $H/E \sim 0.028 > 0.022$ and exhibit sink-in behavior that features a negative correlation between pileup height and scratch depth.

The formation of pileups during indentation is the consequence of dislocations traversing to the surface. Sink-in during indentation generally results from dislocations not being able to reach the surface which can arise from a higher hardening rate of the substrate material that can result from numerous mechanisms [43]. However, the mechanics of formation of pileup (or sink-in) during nanoscratching are more complex than that of indentation. Here, the leading pileup also presumably contributes to side pileups when it is pushed out of the way of the incoming indenter during the process of scratching, and this mechanism is potentially further complicated by nano-meter scale friction effects [44–46]. Kareer et al. have also characterized the lattice rotation field that results in the vicinity of the initial indent (due to normal motion of the indenter), and critically analyzed that with respect to the lattice rotational field in the rest of the scratch (due to lateral motion of the indenter) [1] and have found significant differences. These results underscore the need for more controlled studies for deconvoluting mechanisms of material deformation during nanoscratching.

6. Conclusion

In this work, the mechanism of pileup formation during nano-scratches was studied in the nickel superalloy Inconel 718 which was produced using LPBF. Nano-scratches were produced in the as-received, and solution-annealed states. The pileup heights that were measured using atomic force microscopy of the scratches exhibited a positive correlation with scratch depth in the as-received state. However, these pileups exhibited a negative correlation in their height with the scratch depth in the heat-treated state. By analysis of scratch profiles and potential microstructural differences across as-received, and solution-annealed states of IN718, it was proposed that the changes in pileup formation behaviors result from corresponding changes in their hardening behaviors. The δ precipitates in the H+SA specimen appear to be effective at trapping dislocations before they are able to reach the surface to produce pileups. These δ precipitates also produced marginally larger valley roughness, and likely resulted in a larger resistance of the substrate to scratching that manifested large lateral reaction forces.

Declaration of competing interest

The authors declare that they have no known competing financial interests or personal relationships that could have appeared to influence the work reported in this paper.

Data availability

Data will be available upon request from the corresponding author, upon completion of the project.

Acknowledgments

This material is based upon work supported by the National Science Foundation, United States under Grant No. 1825686. Any opinions, findings, conclusions or recommendations expressed in this material are those of the authors and do not necessarily reflect the views of the National Science Foundation. The authors are also grateful to Dr. Todd Palmer, Dr. Prakash Chakraborty, Dr. Tim Tighe (at Penn State University), Dr. Wendelin Wright (at Bucknell University), Dr. Jessica Cheng (at University of Pittsburgh), and Prof. Dr. mont. Christoph Kirchlechner (at Karlsruhe Institute of Technology) for fruitful conversations. We are also grateful to the reviewer for thoughtful comments that made this manuscript stronger.

References

[1] Anna Kareer, Edmund Tarleton, Christopher Hardie, Sarah V Hainsworth, Angus J Wilkinson, Scratching the surface: Elastic rotations beneath nanoscratch and nanoindentation tests, Acta Mater. 200 (2020) 116–126.

[2] Chen Li, Feihu Zhang, Xin Wang, Xiaoshuang Rao, Repeated nanoscratch and double nanoscratch tests of Lu2o3 transparent ceramics: Material removal and deformation mechanism, and theoretical model of penetration depth, J. Euro. Ceram. Soc. 38 (2) (2018) 705–718.

[3] Yao Chen, Srinivasa R. Bakshi, Arvind Agarwal, Correlation between nanoindentation and nanoscratch properties of carbon nanotube reinforced aluminum composite coatings, Surf. Coat. Technol. 204 (16–17) (2010) 2709–2715.

[4] Lin Huang, Cecile Bonifacio, Da Song, Klaus van Benthem, Amiya K Mukherjee, Julie M Schoenung, Investigation into the microstructure evolution caused by nanoscratch-induced room temperature deformation in M-plane sapphire, Acta Mater. 59 (13) (2011) 5181–5193.

[5] Liye Huang, Jian Lu, Kewei Xu, Elasto-plastic deformation and fracture mechanism of a diamond-like carbon film deposited on a Ti–6Al–4V substrate in nano-scratch test, Thin Solid Films 466 (1–2) (2004) 175–182.

[6] Yu Gao, Carlos J Ruestes, Diego R Tramontina, Herbert M Urbassek, Comparative simulation study of the structure of the plastic zone produced by nanoindentation, J. Mech. Phys. Solids 75 (2015) 58–75.

[7] J. Rodriguez, M.A. Garrido Maneiro, A procedure to prevent pile up effects on the analysis of spherical indentation data in elastic–plastic materials, Mech. Mater. 39 (11) (2007) 987–997.

[8] J.D. Gale, A. Achuthan, The effect of work-hardening and pile-up on nanoindentation measurements, J. Mater. Sci. 49 (14) (2014) 5066–5075.

[9] Roger Smith, D Christopher, Steven D Kenny, Asta Richter, Bodo Wolf, Defect generation and pileup of atoms during nanoindentation of fe single crystals, Phys. Rev. B 67 (24) (2003) 245405.

[10] Clement Keller, E. Hug, Kocks-mecking analysis of the size effects on the mechanical behavior of nickel polycrystals, Int. J. Plast. 98 (2017) 106–122.

[11] Claire Chisholm, Hongbin Bei, MB Lowry, Jason Oh, SA Syed Asif, OL Warren, ZW Shan, Easo P George, Andrew M Minor, Dislocation starvation and exhaustion hardening in Mo alloy nanofibers, Acta Mater. 60 (5) (2012) 2258–2264.

[12] Dan Mordehai, Michael Kazakevich, David J Srolovitz, Eugen Rabkin, Nanoindentation size effect in single-crystal nanoparticles and thin films: A comparative experimental and simulation study, Acta Mater. 59 (6) (2011) 2309–2321.

[13] Ning Xu, Weizhong Han, Yuchun Wang, Ju Li, Zhiwei Shan, Nanoscratching of copper surface by CeO2, Acta Mater. 124 (2017) 343–350.

[14] Shang Sui, Hua Tan, Jing Chen, Chongliang Zhong, Zuo Li, Wei Fan, Andres Gasser, Weidong Huang, The influence of laves phases on the room temperature tensile properties of Inconel 718 fabricated by powder feeding laser additive manufacturing, Acta Mater. 164 (2019) 413–427.

[15] Fencheng Liu, Feiyue Lyu, Fenggang Liu, Xin Lin, Chunping Huang, Laves phase control of inconel 718 superalloy fabricated by laser direct energy deposition via δ aging and solution treatment, J. Mater. Res. Technol. 9 (5) (2020) 9753–9765.

[16] Mohammad Javad Sohrabi, Hamed Mirzadeh, Mohsen Rafiei, Solidification behavior and Laves phase dissolution during homogenization heat treatment of Inconel 718 superalloy, Vacuum 154 (2018) 235–243.

[17] Yang Gao, Dongyun Zhang, Ming Cao, Runping Chen, Zhe Feng, Reinhart Poprawe, Johannes Henrich Schleifenbaum, Stephan Ziegler, Effect of δ phase on high temperature mechanical performances of Inconel 718 fabricated with SLM process, Mater. Sci. Eng. A 767 (2019) 138327.

[18] Mustafa Rifat, Edward C. DeMeter, Saurabh Basu, Microstructure evolution during indentation of Inconel-718 created by additive manufacturing, Mater. Sci. Eng. A (2020) 139204.

[19] Ming Cao, Dongyun Zhang, Yang Gao, Runping Chen, Guoliang Huang, Zhe Feng, Reinhart Poprawe, Johannes Henrich Schleifenbaum, Stephan Ziegler, The effect of homogenization temperature on the microstructure and high temperature mechanical performance of SLM-fabricated IN718 alloy, Mater. Sci. Eng. A 801 (2021) 140427.

[20] SAE Aerospace, Aerospace material specification: AMS 5662, SAE Int. (2009).

[21] W.C. Liu, Mei Yao, Z.L. Chen, S.G. Wang, Niobium segregation in Inconel 718, J. Mater. Sci. 34 (11) (1999) 2583–2586.

[22] GH Cao, TY Sun, CH Wang, Xing Li, M Liu, ZX Zhang, PF Hu, Alan M Russell, R Schneider, DJMC Gerthsen, et al., Investigations of γ', γ and δ precipitates in heat-treated Inconel 718 alloy fabricated by selective laser melting, Mater. Charact. 136 (2018) 398–406.

[23] Nicholas C. Ferreri, Sven C. Vogel, Marko Knezevic, Determining volume fractions of γ, γ', γ'', δ, and MC-carbide phases in Inconel 718 as a function of its processing history using an advanced neutron diffraction procedure, Mater. Sci. Eng. A 781 (2020) 139228.

[24] Ariane Iturbe, Eliane Giraud, Exabier Hormaetxe, Ainhara Garay, Guénaël Germain, Koldo Ostolaza, Pedro José Arrazola, Mechanical characterization and modelling of Inconel 718 material behavior for machining process assessment, Mater. Sci. Eng. A 682 (2017) 441–453.

[25] Florian Bachmann, Ralf Hielscher, Helmut Schaeben, Grain detection from 2d and 3d EBSD data-specification of the MTEX algorithm, Ultramicroscopy 111 (12) (2011) 1720–1733.

[26] Wolfgang Pantleon, Resolving the geometrically necessary dislocation content by conventional electron backscattering diffraction, Scr. Mater. 58 (11) (2008) 994–997.

[27] Amit Acharya, Robin J. Knops, An observation on the experimental measurement of dislocation density, J. Elasticity 114 (2014) 275–279.

[28] Sepideh Abolghasem, Saurabh Basu, M. Ravi Shankar, Quantifying the progression of dynamic recrystallization in severe shear deformation at high strain rates, J. Mater. Res. 28 (15) (2013) 2056–2069.

[29] JC Stinville, MA Charpagne, A Cervellon, S Hemery, F Wang, PG Callahan, V Valle, TM Pollock, On the origins of fatigue strength in crystalline metallic materials, Science 377 (6610) (2022) 1065–1071.

[30] Boštjan Taljat, George Mathews Pharr, Development of pile-up during spherical indentation of elastic–plastic solids, Int. J. Solids Struct. 41 (14) (2004) 3891–3904.

[31] K.W. McElhaney, Joost J. Vlassak, William D. Nix, Determination of indenter tip geometry and indentation contact area for depth-sensing indentation experiments, J. Mater. Res. 13 (5) (1998) 1300–1306.

[32] C. Anthony, Fischer-cripps, nanoindentation, 2011.

[33] David J. Shuman, André L.M. Costa, Margareth S. Andrade, Calculating the elastic modulus from nanoindentation and microindentation reload curves, Mater. Charact. 58 (4) (2007) 380–389.

[34] William D. Nix, Huajian Gao, Indentation size effects in crystalline materials: a law for strain gradient plasticity, J. Mech. Phys. Solids 46 (3) (1998) 411–425.

[35] P.J. Apps, M. Berta, P.B. Prangnell, The effect of dispersoids on the grain refinement mechanisms during deformation of aluminium alloys to ultra-high strains, Acta Mater. 53 (2) (2005) 499–511.

[36] AP.G.M. Bolshakov, G.M. Pharr, Influences of pileup on the measurement of mechanical properties by load and depth sensing indentation techniques, J. Mater. Res. 13 (4) (1998) 1049–1058.

[37] Yang-Tse Cheng, Che-Min Cheng, Scaling, dimensional analysis, and indentation measurements, Mater. Sci. Eng. R 44 (4–5) (2004) 91–149.

[38] F.J. Lockett, Indentation of a rigid/plastic material by a conical indenter, J. Mech. Phys. Solids 11 (5) (1963) 345–355.

[39] HW Zhang, G Subhash, XN Jing, LJ Kecskes, RJ Dowding, Evaluation of hardness–yield strength relationships for bulk metallic glasses, Phil. Mag. Lett. 86 (5) (2006) 333–345.

[40] V. Marx, H. Balke, A critical investigation of the unloading behavior of sharp indentation, Acta Mater. 45 (9) (1997) 3791–3800.

[41] Peter Burik, Ladislav Pešek, Lukáš Voleský, Effect of pile-up on the mechanical characteristics of steel by depth sensing indentation, in: Key Engineering Materials, vol. 606, Trans Tech Publ, 2014, pp. 81–84.

[42] Muhammad Hassaan, Massab Junaid, Tauheed Shahbaz, Muhammad Ilyas, Fahd Nawaz Khan, Julfikar Haider, Nanomechanical response of pulsed tungsten inert gas welded titanium alloy by nanoindentation and atomic force microscopy, J. Mater. Eng. Perform. 30 (2021) 1490–1503.

[43] Frederick John Humphreys, Max Hatherly, Recrystallization and Related Annealing Phenomena, elsevier, 2012.

[44] Xiaoming Liu, Zhanli Liu, Yueguang Wei, Ploughing friction and nanohardness dependent on the tip tilt in nano-scratch test for single crystal gold, Comput. Mater. Sci. 110 (2015) 54–61.

[45] D. Mulliah, D. Christopher, S.D. Kenny, Roger Smith, Nanoscratching of silver (100) with a diamond tip, Nucl. Instrum. Methods Phys. Res. B 202 (2003) 294–299.

[46] M. Chamani, G.H. Farrahi, M.R. Movahhedy, Friction behavior of nanocrystalline nickel near the Hall-Petch breakdown, Tribol. Int. 107 (2017) 18–24.